Simultaneous, Unsteady PIV and Photogrammetry Measurements of a Tension-Cone Decelerator in Subsonic Flow

Edward T. Schairer[1], James T. Heineck[2], Louise A. Walker[3], Laura K. Kushner[4], Gregory G. Zilliac[5]

1: NASA Ames Research Center, Moffett Field, CA, USA, edward.t.schairer@nasa.gov
2: NASA Ames Research Center, Moffett Field, CA, USA, james.t.heineck@nasa.gov
3: NASA Ames Research Center, Moffett Field, CA, USA, louise.a.walker@nasa.gov
4: NASA Ames Research Center, Moffett Field, CA, USA, laura.k.kushner@nasa.gov
5: NASA Ames Research Center, Moffett Field, CA, USA, gregory.g.zilliac@nasa.gov

Abstract This paper describes simultaneous, synchronized, high-frequency measurements of both unsteady flow in the wake of a tension-cone decelerator in subsonic flow (by PIV) and the unsteady shape of the decelerator (by photogrammetry). The purpose of these measurements was to develop the test techniques necessary to validate numerical methods for computing fluid-structure interactions of flexible decelerators. A critical need for this effort is to map fabric surfaces that have buckled or wrinkled so that code developers can accurately represent them. This paper describes a new photogrammetric technique that performs this measurement. The work was done in support of the Entry, Descent, and Landing discipline within the Supersonics Project of NASA's Fundamental Aeronautics Program.

1. Introduction

Beginning with the Viking Lander in 1976, the United States has relied upon a single technology—disk-gap-band (DGB) parachutes—to decelerate all of its Mars landers from supersonic to subsonic speeds as they enter the Martian atmosphere. The use of Viking parachute technology will culminate with the Mars Science Laboratory (MSL), scheduled to arrive at Mars in 2012. MSL will push DGB technology to its limit in terms of mass of the payload (850 kg), size of the decelerator (21.5 m dia), deployment Mach number (2.3), and length of time (5–10 sec) the parachute operates above Mach 1.5, a speed regime where a parachute instability known as "area oscillations" can occur (Sengupta et al. 2009). Missions more massive than MSL, including manned missions, will require an alternate decelerator technology. Numerical simulation will play a key role in developing new concepts and in reducing the technical risk inherent in deviating from proven DGB technology. Before this is possible, however, numerical tools for computing fluid interactions with very flexible structures must be developed and validated.

Supersonic wind tunnel tests of new decelerator concepts are planned for the NASA Ames 9x7 Ft (2.7 x 2.1 m) Supersonic Wind Tunnel. These tests will include: (1) measurements of unsteady flow both upstream of and in the wake of the decelerator by 3-component particle image velocimetry (PIV); (2) simultaneous, synchronized measurements of the shape of the decelerator by stereo photogrammetry; (3) unsteady force and moment balance data; and (4) high-speed schlieren imaging. One of the challenges of making these measurements is the very restricted optical access through existing windows in the 9x7 Ft Wind Tunnel (Heineck et al. 2005). To help reduce the technical risk in making these measurements, a proof-of-concept test was conducted in the 32- by 48- in (0.81 x 1.22 m) Low-Speed Wind Tunnel in the Ames Fluid Mechanics Laboratory. This test demonstrated simultaneous, synchronized, high-frequency measurements of the unsteady deformation of a decelerator and the unsteady flow in its wake using photogrammetry and PIV systems that replicated as much as possible the systems that will be deployed in the 9x7 SSWT.

2. Experiment

2.1 Wind Tunnel

The 32- ft by 48-in (0.81 x 1.22 m) Low-Speed Wind (Chow et al. 1997) is an in-draft wind tunnel that draws ambient room air through a 9:1 contraction ratio inlet equipped with a honeycomb screen at its upstream end. The walls of the test section are easily modified to accommodate windows to meet the needs of a particular test. For the current test, the sidewalls downstream of a short Plexiglass transition section were plywood, and each supported two 8- by 25-in (0.2 x 0.63 m) optical-quality windows. The floor of the test section included a motor-driven turntable in which was a mounted 0.22 x 0.488 m (8.75 x 19.24-in) optical window. Airspeed in the test section can be adjusted between about 13.7–37 m/s (45 and 120 f/s) by changing the height of a converging-diverging nozzle between the test section from the diffuser. The nozzle is choked during normal operations, thus preventing disturbances from the diffuser and vacuum manifold from propagating upstream into the test section. Vacuum in the manifold downstream of the diffuser is maintained by a large compressor.

2.2 Models

Each of the several models that were built for this test was a "tension-cone" formed by a circular aluminum center-body, a torus formed by an inflated bicycle-tire inner tube, and Teflon-coated nylon fabric that was wrapped around the inner tube and connected it to the center body (Fig. 1). The diameter of the center-body was 100 mm (4 in); the outer diameter of the inner tube was 330 mm (13 in) and its cross-sectional diameter was 32 mm (1.25 in). Sixty-eight retro-reflective targets (diameter = 6.35 mm) that could be tracked by the photogrammetry cameras were glued to the upstream face of the model. One of the models was made using black fabric that was splattered with white paint to create a random distribution of high-contrast speckles that could also be tracked by photogrammetry, permitting full-surface measurements. The model was rigidly supported at the back of the center-body by a balance-instrumented sting that extended downstream to a tripod that was attached to the turntable in the tunnel floor. All tests were conducted with the model axis aligned with the tunnel axis.

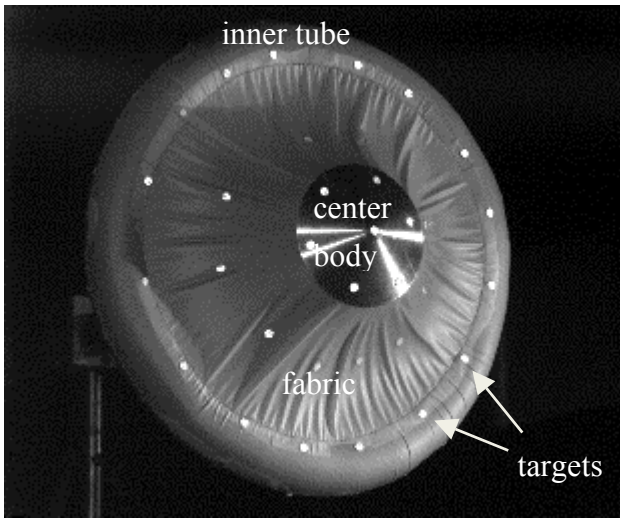

Fig. 1 Tension-cone decelerator model.

2.3 Instrumentation and Data Reduction

Instrumentation consisted of a four-camera photogrammetry system, two independent stereo PIV systems (one for high-frequency measurements in the model wake and the other for measuring inflow conditions), and a balance that supported the models. The photogrammetry and high-frequency PIV cameras were synchronized to acquire images at the same instants.

2.3.1 PIV

The first PIV system made high-frequency measurements (1000 Hz) below the sting and in the wake of the model where the flow was very unsteady (Figs. 2 and 3). The light source was a Spectra-Physics "Quanta Ray" Nd Yag laser that, along with sheet-forming optics, was located under the test section. The laser sheet was projected upward through the window in the floor of the test section in a plane that was aligned with the free-stream flow and rotated 4° from vertical. The sheet was terminated at the sting and was imaged from opposite sides by high-speed cameras (Phototron Fastcam SA1.1, 1024 x 1024 pixels) on opposite sides of the test section. The rotation of the laser sheet and the unfavorable scatter angles were due to constraints imposed by the 9x7 SSWT configuration. Images from both cameras were acquired at 2000 frames per sec, and the integration time for each image was 1/2000 = 500 µs. Pairs of pulses from the laser were timed to occur near the end and beginning of each pair of successive images. The time between each pair of laser pulses was adjusted based on the thickness of the laser sheet (about xx mm) and desired particle displacement (xx pixels). Thus, the particles imaged in successive image pairs were separated in time by the time between laser pulses.

The purpose of the second PIV system was to measure inflow conditions that could be used as boundary conditions for computational fluid dynamic simulations. Since the flow upstream of the model was very steady, it was not necessary to acquire data at a high rate, and the PIV and

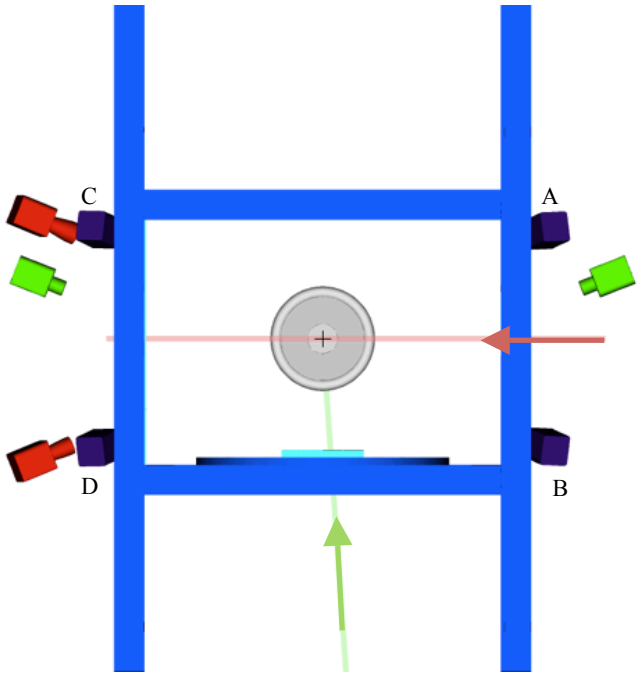

Fig. 2 View of test section from upstream. Green is high-speed PIV; red is inflow PIV; purple is photogrammetry cameras (A-D).

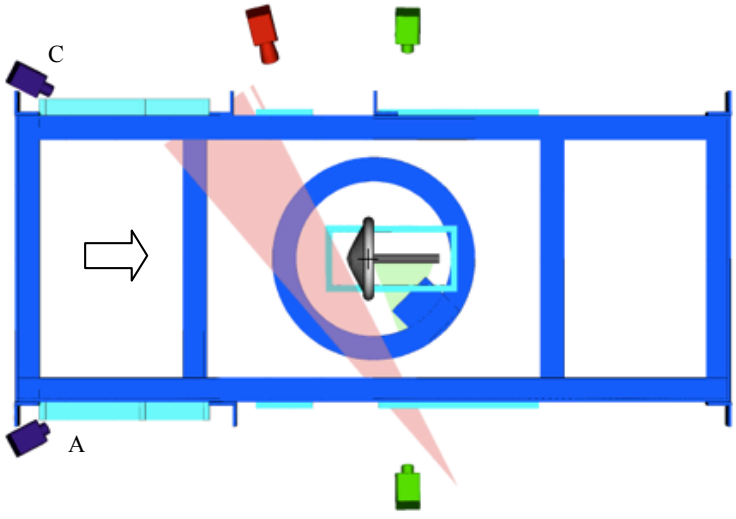

Fig. 3 Top view of test section showing PIV and photogrammetry systems.

photogrammetry systems were not synchronized for these measurements. Instead, measurements were made at higher spatial resolution and much lower data rate (7 Hz) using Princeton Instruments MegaPlus ES 4020 cameras (2048 x 2048 pixels). The laser sheet was projected through a window in one sidewall in a horizontal plane just upstream of the model. It was imaged in forward scatter from above and below by the two cameras positioned on the opposite side of the test section as the laser (Figs. 2 and 3).

The PIV cameras were calibrated using the Soloff (1997) volumetric method. A flat calibration plate with a rectangular array of targets was placed in the measurement plane and displaced in small steps in the direction normal to its surface, and at each position an image was acquired by both cameras. The flow was seeded with droplets of mineral oil sprayed from a nozzle upstream of the inlet. Relatively large droplets (approx xx microns) were required to produce useable signals for measurements in the wake because of the large scatter angles to the cameras. Seed in the recirculation zone on the lee side of the model was considerably sparser than in the shear layer at the edges of the model.

The PIV images were analyzed by standard methods using in-house data-reduction software. A rectangular interrogation grid that lay in the measurement plane was defined in object space and was projected into the images of both cameras using the camera calibration coefficients. At each instance, images from both cameras were mapped to the measurement plane ("de-warped") and cross correlated with each other at each measurement point to determine the local offset, if any, between points in the images of the two cameras due to vibration or misalignment. This insured that displacement measurements were made on the same particles in the images of both cameras (Willert 1997).

2.3.2 Photogrammetry

The upstream face of the model was imaged by four photogrammetry cameras (Redlake Motion Pro X3 Plus, 1280 x 1024 pixels) that were synchronized to the high-frequency PIV cameras. The cameras were positioned symmetrically, two on each side of the test section, one high looking slightly down and the other low looking slightly up (Figs. 2 and 3). The cameras were calibrated by imaging a "ziggurat"-- a stack of five concentric, progressively smaller circular disks with targets marked on each step (Fig. 4)--that was installed in place of the model before and after the test. Targets on the ziggurat spanned the region of space that the model occupied. The Direct Linear Transformation (DLT, Karara and Abdel-Aziz 1974) was computed for each camera from the image- and object-space coordinates of the targets. The model and ziggurat were continuously illuminated by four high-intensity lamps, one near each camera.

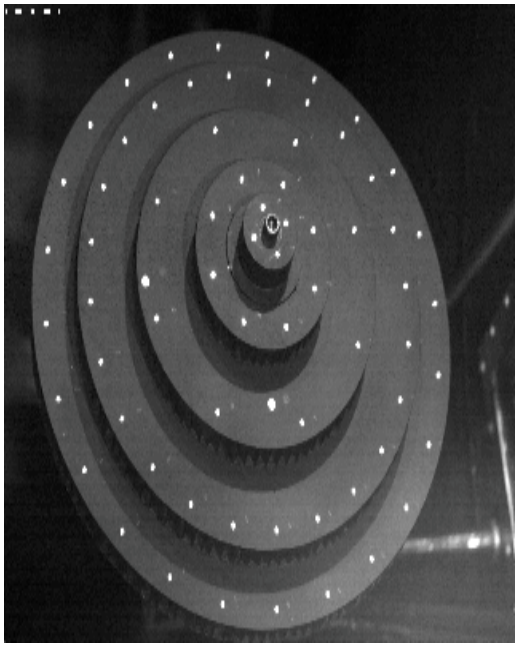

Fig. 4 Ziggurat for calibrating photogrammetry cameras.

The photogrammetry data were analyzed in two ways using custom in-house software. By the first method—"target-tracking"—the retro-reflective targets that were glued to the fabric of the tension cone were tracked through the image sequence from each camera. Targets were located in the first image from each camera by "point and click" with the computer mouse. These positions were refined with a

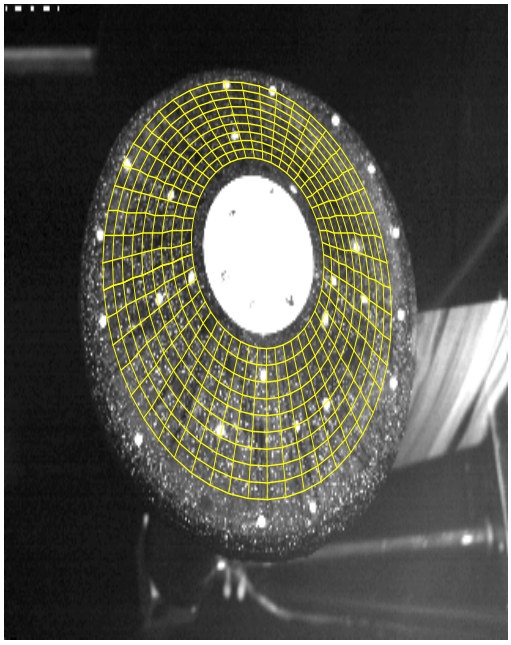

Fig. 5 Black model speckled with white paint with grid overlay.

centroid-finder in an interrogation window centered on the position of each target. Targets were tracked in subsequent images using either the same centroid finder or by cross correlating image data in each interrogation window with data from the first image—both methods yielded essentially the same result. The spatial resolution of this method was limited by the number and distribution of targets on the model and by the size of the interrogation window used to track each target. Correspondence of targets between images from the several cameras (i.e., the condition that all cameras are measuring the position of the same target) was unambiguous as long as targets were not so close together that more than one target appeared in each interrogation window.

The second method--"full-surface photogrammetry"--used the Photogrammetric Recession Measurement (PRM) algorithm (Schairer and Heineck 2010) to track local speckle patterns and did not require targets. Instead, a surface grid that approximated the shape of the fabric portion of the model was projected into the image of each camera using the camera calibration coefficients (Fig. 5). The unique splatter pattern at each node was tracked through the sequence of images by cross correlation just as if it were a retro-reflective target. Correspondence of points between cameras was enforced by cross correlating local data from the second, third, and fourth cameras (B, C, and D) with corresponding data from the first camera (A). This required first locally "de-warping" each interrogation window to eliminate perspective distortion. Unlike "global de-warp" transformations that are used in PIV to ensure correspondence of measurement points in a plane (Willert 1997), this procedure required a different transformation at each node of the grid and allowed for non-planar measurement surfaces. Because the speckle pattern on the model remained unchanged throughout each run, correspondence of measurement points had to be established only in the first image from each camera. Thereafter, the nodes of the grid were tracked independently in the image sequence from each camera; in each image, data within a small interrogation window at each node were cross-correlated with data at the same node from the first image in the sequence from the same camera. This was a simplification of the algorithm that was developed for arcjet applications, where the texture of the model changes continuously and correspondence must be enforced by camera-to-camera cross correlation in each image of the sequence. With the PRM algorithm, spatial resolution is set by the densities of the speckles and surface grid and is limited by the size of the interrogation window used for cross correlation.

The object-space position of each measurement point—targets in the first analysis method and grid nodes in the second—was computed from the image-plane coordinates of the point and the DLT coefficients from at least two cameras. Each camera contributed two equations (one each for X and Y) to an over-determined linear set that was solved in a least-squares sense for the object-space coordinates x, y, and z. Each calculation could include data from two, three, or four cameras; however, the uncertainty of the result is minimized by including only data from the two cameras for which the uncertainty in locating the target in the images is least. For the PRM algorithm, this was the reference camera (A) and the camera for which the signal-to-noise ratio (SNR) of the local camera-to-camera (B-to-A, C-to-A, or D-to-A) cross correlation function was largest. [SNR was defined as the ratio of the peak of the cross-correlation function to the standard deviation of the function within the interrogation window.] In principle, this could be different for each

measurement point depending on the local orientation of the model surface relative to the cameras. In practice, the best two cameras were usually the reference camera (A) and the other camera on the same side of the test section as camera A (camera B).

For the "target-tracking" analysis method, displacement of the model at points between the irregularly distributed targets was interpolated using a "natural neighbor interpolation" algorithm that was implemented in a MatLab script. This produced, at each time step, displacement data on a regular, rectangular grid. Interpolated displacement data for the entire data sequence were written to a Tecplot file.

3. Results and discussion

Photogrammetry and PIV measurements are presented for a single case where the freestream velocity was 15.2 m/s (50 ft/s). To the naked eye the position and shape of the model appeared very steady once run conditions had been established. The model was black and had been speckled with white paint. Many of targets, which were glued to the model fabric, had fallen off in previous runs leaving voids where there were neither targets nor speckles. PIV measurements were made both upstream of the model and in its wake; however, only wake measurements are presented here. The upstream measurements from the second PIV system, though important for CFD simulations and to the planning and execution of the experiment, were not otherwise very interesting. Synchronized bursts of images were acquired by the high-speed PIV and photogrammetry systems. The photogrammetry cameras acquired images at 500 Hz for one second; each PIV camera acquired pairs of images (initial and delay) at 1000 Hz for 0.5 sec. Times are given in ms from the beginning of the data burst.

The position of the high-speed PIV measurement region relative to the model is shown in Fig. 6, where the model and a single sequence of data are presented. Most of the measurement region was in the model wake, but the lower edge extended below the model into the shear layer and free stream. Four sequential instances of PIV data separated by 1 ms are shown in Fig. 7. The color contour shows streamwise velocity, and the vector overlay indicates flow angle. Flow below the lower edge of the model has been accelerated relative to the freestream, and there is a large recirculation zone of low-velocity air in the wake of the model. The data sequence clearly shows the convection of large flow structures, including a vortex in the recirculation zone, indicating that large-scale flow unsteadiness, which is likely most important for understanding fluid-structure interactions, has been resolved.

The first image from each of the four photogrammetry cameras is shown in Fig. 8. Each image includes a surface grid formed by a conical frustum whose parameters were adjusted by trial-and-error to give a good fit to the fabric portion of the model. The grid consists of 100 x 25 = 2500 nodes. Each node in camera A overlies a unique splatter pattern on the model that became a virtual target. Corresponding nodes in the first images from cameras B, C, and D were found by camera-to-camera cross correlation as described above.

The increase in spatial resolution that the full-surface method yields compared to the target-tracking method is illustrated in Fig. 9, which

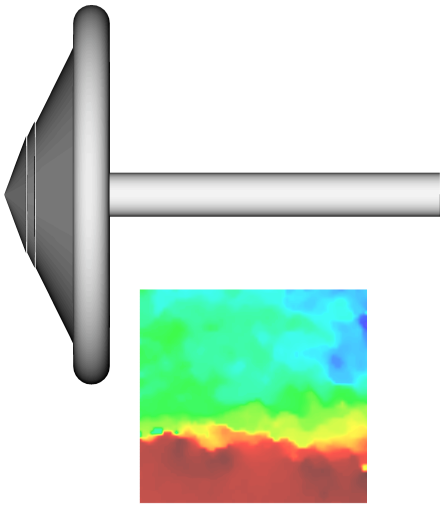

Fig. 6 Location of high-speed PIV measurement region.

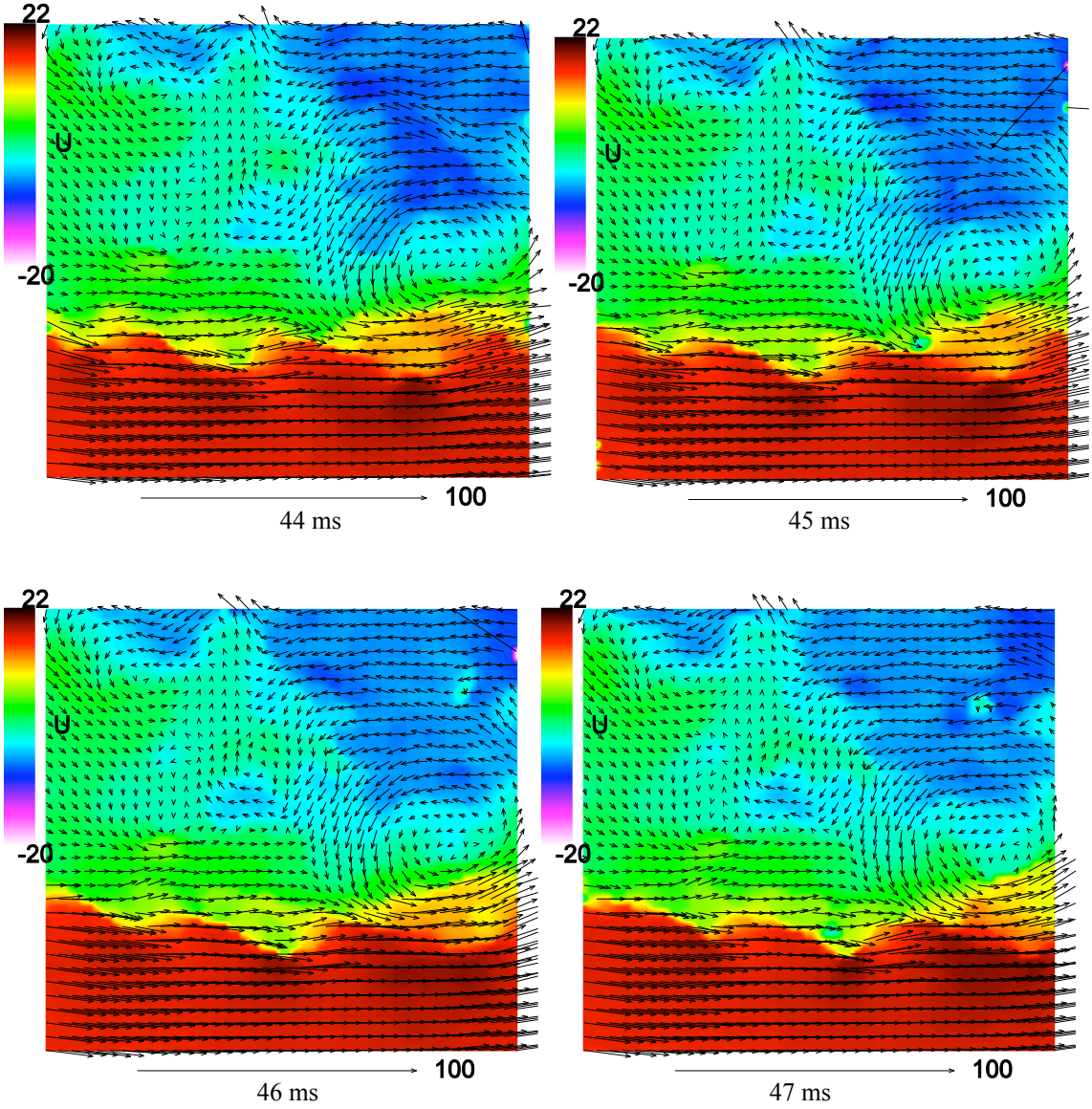

Fig. 7 High-frequency PIV data at consecutive 1 ms intervals. Color contour shows streamwise velocity; vectors show flow angle.

compares axial displacement distributions at the same instant (96 ms) determined by the two methods. The trends are very similar, but the full-surface method (left) clearly provides spatial variations that are lost in the target finding method (right).

Fig. 10 shows images of the model at two instances 78 msec (39 frames) apart. Each image has been overlaid with a color contour map showing the local axial displacement measured by the full-surface method. The displacements are very small—maximum displacements are less than two mm near the edges of the model. Note that the displacements near the edges of the model have changed signs between the two instances.

Time histories of the displacements of two nodes at the same radius but near opposite edges of the model (indicated in Fig. 10) are shown in Fig. 11. Both time histories are periodic with a frequency of about 7 Hz, and there is a phase difference of about 180 degrees between them. This phase difference is further illustrated in Fig. 12, which shows the axial displacements of a circumferential set of targets near the edge of the model at three instants in time. At all three times,

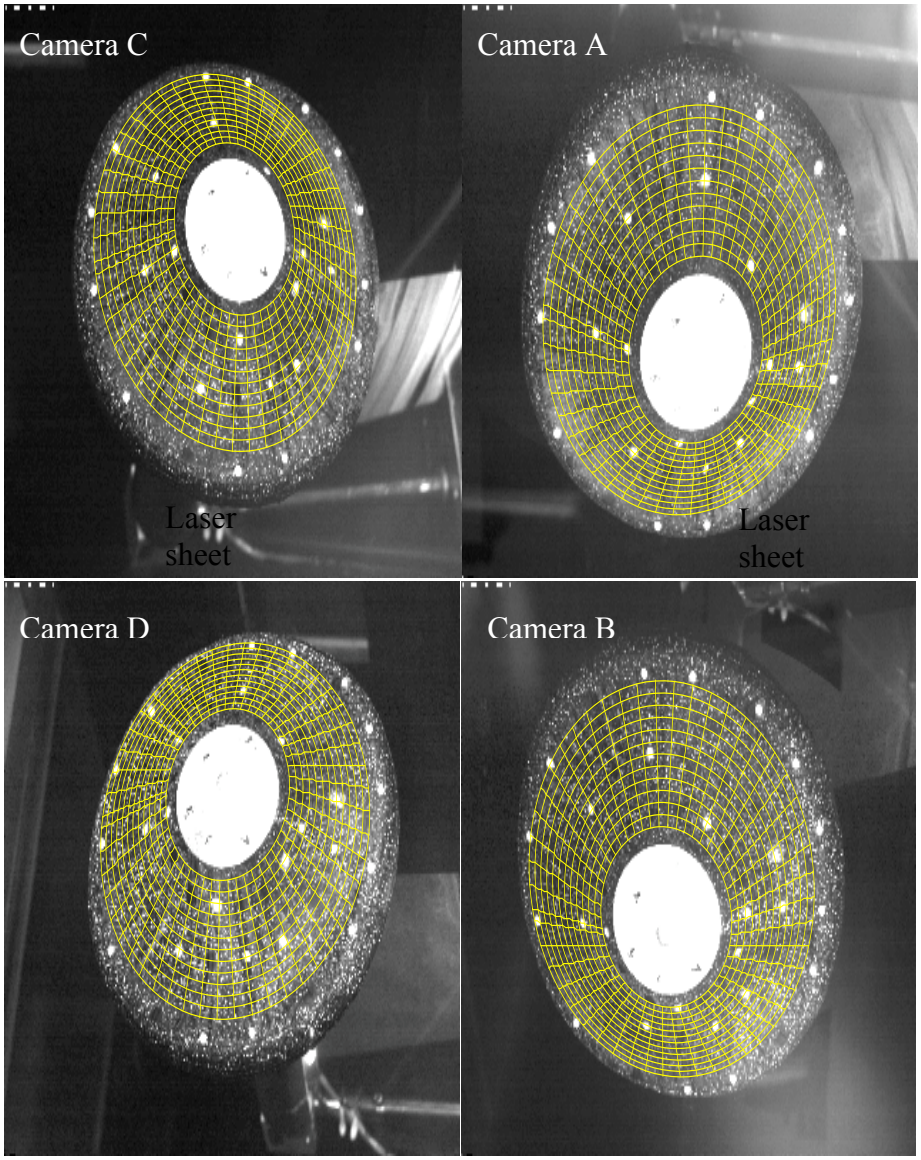

Fig. 8 Images from the photogrammetry cameras showing model, laser sheet, and full-surface interrogation grid. Only every other grid node is shown.

the largest displacements occur at azimuth angles of about 120 and 300 degrees, where the displacements are in opposite directions. Near azimuth angles 20 and 200 degrees displacements are nearly zero at all three times. This indicates the model is rocking about the 20-200 degree axis. Fig. 13 shows the displacement of virtual targets along a radial line at four times. It shows that displacements along the line increase with distance from the model axis and that the points along the line are in phase with each other--at least near the edge of the model where displacements are largest. It is more difficult to ascertain phase differences at inboard points where the displacements are much smaller.

The uncertainty of the PIV and photogrammetry measurements depended mostly on the uncertainty in measuring image-plane displacements of seed particles for PIV and speckle patterns or targets for photogrammetry. The corresponding object space uncertainty depends on the relative geometry between the cameras and measurement points, as represented by the calibration transformations. For the photogrammetry system, the greater separation between cameras A and C (located on opposite sides of the wind tunnel) compared to A and B (on the same side, separated vertically—see Fig. 2) resulted in greater sensitivity of the AC combination to axial (streamwise) displacements. [By symmetry, the same can be said of the combination BD relative to CD]. However, an undesirable effect of this greater separation was to increase the difference in perspective between the cameras, which increased the uncertainty in the camera-to-camera cross correlation that was used to enforce correspondence of measurement points for the full-surface method. Therefore, for the full-surface method, the uncertainty in measuring image-plane displacements of corresponding points was greater for AC than for AB, and this uncertainty more than offset the advantage of the AC geometry.

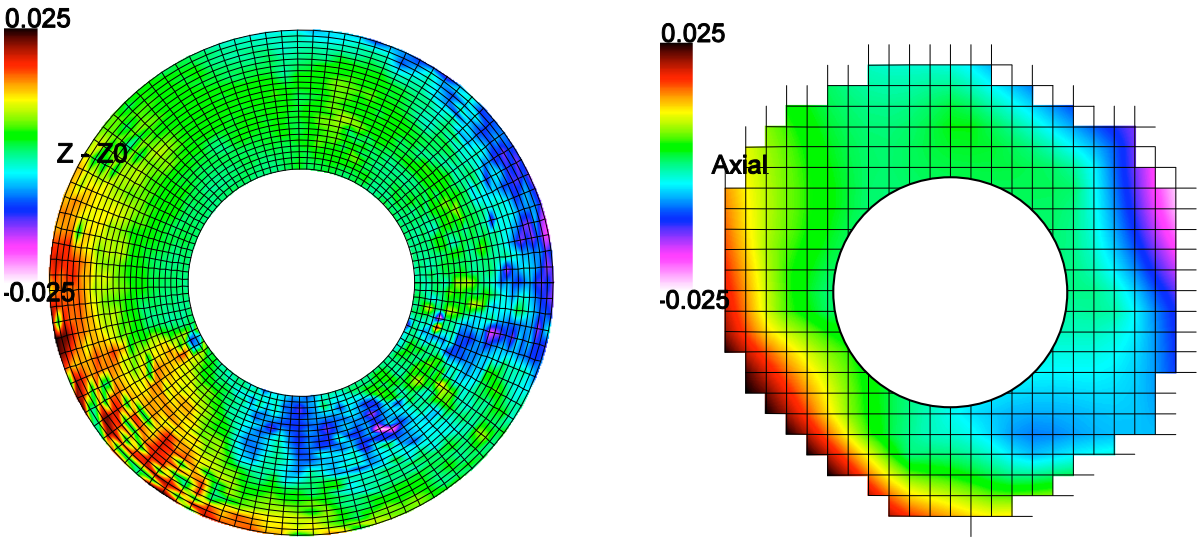

Fig. 9 Comparison of axial displacement distributions computed from full-surface (left) and by interpolating measurements at targets (right). Time = 96 ms.

Because photogrammetry data were acquired with more than two cameras, one way to assess uncertainty is to compare displacements measured by different combinations of cameras. With the target-tracking method, axial displacements computed from combinations of two, three, and four cameras were consistent to within 0.1 mm at most points. This mostly reflects uncertainty in the DLT transformations because the correspondence of targets between the cameras was unambiguous.

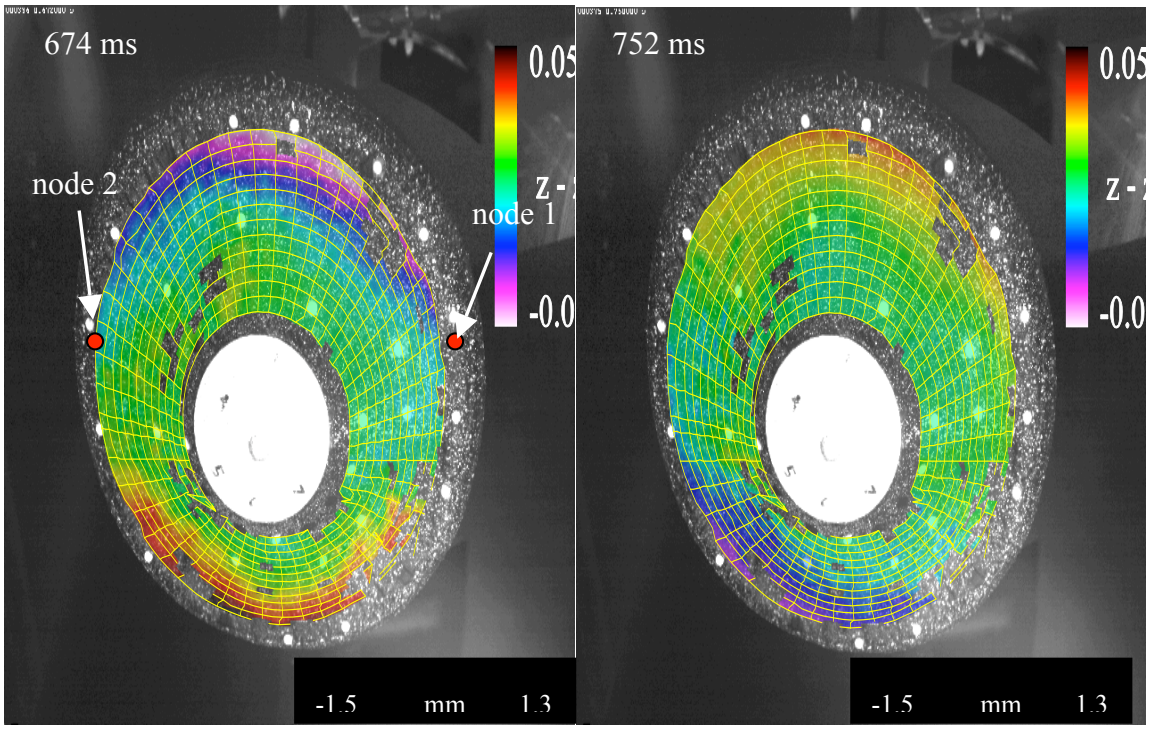

Fig.10 Axial displacement measurements at two times separated by 78 ms. Time histories of nodes 1 and 2 are shown in Fig. 11.

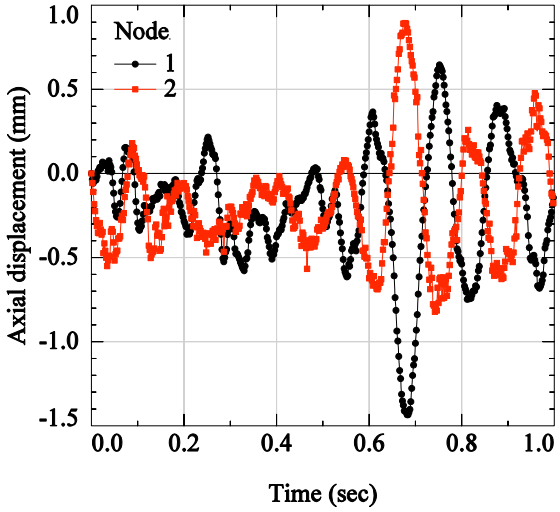

Fig. 11 Time histories of axial displacements at two points.

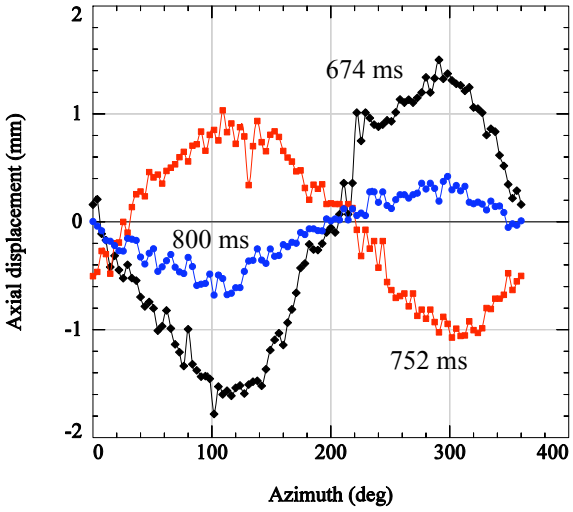

Fig. 12 Axial displacements of points near edge of model at three times.

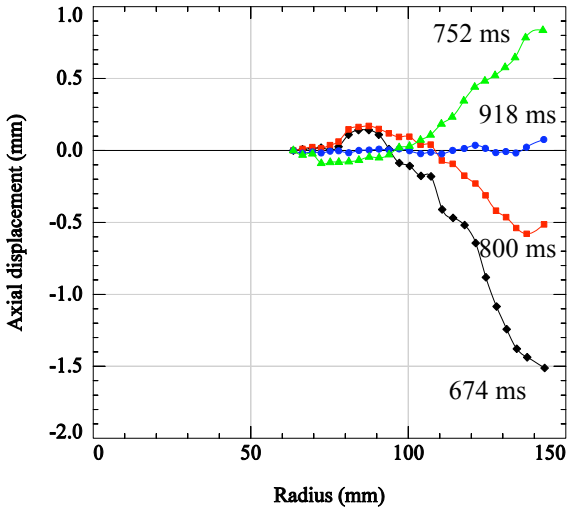

Fig. 13 Axial displacement along a radial line at four times.

For the full-surface method, however, the uncertainty in establishing correspondence by camera-to-camera cross correlation increased with increasing separation between cameras. Therefore, all of the full-surface measurements reported here are based on data from cameras A and B.

For this combination, an uncertainty of ±1 pixel in measuring the image-plane displacement of a corresponding point in the images of both cameras led to a maximum uncertainty in axial displacement of about 3 mm. Thus a ±0.1 pixel uncertainty, a realistic estimate, corresponded to about 0.3 mm in axial displacement. The data in Fig. 11 suggest that cameras A and B were resolving smaller axial displacements than this.

4. Conclusions

The experiment successfully demonstrated simultaneous, synchronized measurements of both the high-frequency variations in the shape of a flexible model and the unsteady flow in the model's wake. Measurements of this type will be required to validate computer codes for predicting the performance of the new types of decelerators that are needed for future missions to Mars. The PIV measurements resolved large scale flow unsteadiness in the model's wake. Photogrammetry measurements of changes in the model shape were made at nearly 2500 points by adapting the Photogrammetric Recession Measurement technique, which was developed for measuring the recession of thermal-protection system materials in arcjets, to the current application. Although the method was extended to allow including data from up to four cameras, the best results were achieved using data from the two best cameras.

References

Chow, J, Zilliac, G, Bradshaw, P (1997) Turbulence Measurements in the Near Field of a Wingtip Vortex. NASA TM-110418, February 1997

Heineck, JT, Schairer, ET, and Walker, SM (2005) PIV Measurements of Flow Past the Space Shuttle Ascent Configuration in the NASA Ames 9- by 7-Foot Supersonic Wind Tunnel. In: Proceedings of the 6th International Symposium on Particle Image Velocimetry (PIV 2005), Pasadena, CA, September 21–23, 2005

Karara, HM, and Abdel-Aziz, YI (1974) Accuracy Aspects of Non-Metric Imageries. Photogrammetric Engineering, 40(7)1107–1117

Schairer, ET and Heineck, JT (2010) Photogrammetric Recession Measurements of Ablative Materials in Arcjets. Meas Sci Technol 21: 025304

Schairer, ET, Heineck, JT, Walker, SM, and Yaste, DM (2005) Predicting Camera Views for Image-Based Measurements in Wind Tunnels. Presented at: 43rd AIAA Aerospace Sciences Meeting and Exhibit, Reno, NV, Jan. 10–13, 2005, paper 2005-1349

Sengupta, A, Steltzner, A, Witkowski, A, Candler, G, and Pantano, C (2009) Findings from the Supersonic Qualification Program of the Mars Science Laboratory Parachute System. Presented at: 20th AIAA Aerodynamic Decelerator Systems Technology Conference and Seminar, Seattle, WA, May 4–7, 2009, paper 2009-2900

Soloff, SM, Adrian, RJ, and Liu, Z-C (1997) Distortion Compensation for Generalized Stereoscopic Particle Image Velocimetry. Meas Sci Technol 8:1441–1454

Willert, C (1997) Stereoscopic Digital Particle Image Velocimetry for Application in Wind Tunnel Flows. Meas Sci Technol 8:1465–1479